COMMUNICATION

The lead(II)–*N*′-isonicotinoylpyrazine-2-carbohydrazonamide complex system as a converter of aerial carbon dioxide to carbonate under electrochemical conditions with the formation of a single-component white light-emitting phosphor†

Received 00th January 20xx,
Accepted 00th January 20xx

DOI: 10.1039/x0xx00000x

Ghodrat Mahmoudi,*[a,b,c] Isabel Garcia-Santos,*[d] Elena Labisbal,[d] Alfonso Castiñeiras,[d] Vali Alizadeh,[e] Rosa M. Gomila,[f] Antonio Frontera[f] and Damir A. Safin*[g,h]

In this contribution, a novel binuclear heteroleptic complex $[Pb_2L_2(CO_3)]\cdot 2CH_3CN\cdot 2MeOH$ (**1**·$2CH_3CN$·2MeOH) is reported, which was fabricated by electrochemical oxidation of a lead anode under the ambient atmosphere in a CH_3CN:MeOH solution of *N*′-isonicotinoylpyrazine-2-carbohydrazonamide (**HL**). The CO_3^{2-} anion was produced from conversion of the aerial CO_2 by the Pb^{2+}–**L** complex system under electrochemical conditions. In the structure of **1**, the ligands **L** exhibit a tridentate pincer-like *N*,*N*′,*O*-coordination mode, while the CO_3^{2-} anion exhibits a tetradentate bridging coordination mode with one of the oxygen atoms exhibiting a bridging μ-coordination mode. The metal cations in the structure of **1** are in a five-membered N_2O_3 coordination environment, formed by the covalent bonds. The molecular structure of **1**·$2CH_3CN$·2MeOH is stabilized by a pair of intermolecular Pb···N tetrel bonds formed with one of the NH_2 nitrogen atoms of an adjacent complex molecule and with the acetonitrile nitrogen atom, and one Pb···O tetrel bond formed with the carbonyl oxygen atom of the other adjacent complex molecule, yielding a 2D supramolecular sheet. This sheet is further stabilized by intermolecular N–H···$N_{acetonitrile}$ and N–H···$O_{carbonate}$ hydrogen bonds, and $\pi_{Prz}\cdots\pi_{Py}$ interactions. The optical properties of complex were revealed by UV-vis spectroscopy and spectrofluorimetry in MeOH. It was established that the described complex is emissive upon excitation at 340 nm with a broad band from about 500 nm to 780 nm with a maximum at ~580 nm, accompanied with a shoulder at ~620 nm. The CIE-1931 chromaticity coordinates of (0.28, 0.36) fall within the white gamut of the chromaticity diagram. Thus, complex **1** is a single-component white light-emitting phosphor.

1. Introduction

Nowadays, it is hard to overestimate a crucial role of carbon dioxide (CO_2) as one of the dominant contributors to exacerbated global warming.[1–3] However, despite its obvious negative influence, CO_2 is of potential interest as an abounding source of carbon toward a great variety of product of value. This is even more important considering an imminent decline in readily available oil and natural gas reserves. While CO_2 is of potential interest as an abundant and readily available source of carbonate and hydrocarbon derivatives, it is a highly stable molecule, which conversion to the products of value requires specific conditions and, usually, proceeds under catalytic conditions. Of a numerous different approaches, fabrication of the value-added carbon-containing compounds upon chemical activation of CO_2 seems to be one of the most attractive procedure to overcome this problem. In this regard, using metal-containing compounds has become one of the most efficient approaches for activation of inert molecules, including CO_2.[4–6] By varying experimental conditions, CO_2 can be transformed to a broad variety of compounds: CO, carbonate, carbamate, methane, formaldehyde, formic acid, methanol, etc.[4–6] It is supposed that CO_2 is activated through the reduction to the highly active $CO_2^{\cdot-}$ radical anion, which formation proceeds under great negative potentials.[7–9] This is explained by both the formation of high-energy intermediates, and a large energy required to change the linear geometry to a bent structure. As such, experimental conditions can dictate these transformations and influence on the resulting potentials, facilitating the CO_2 activation.

[a] Department of Chemistry, Faculty of Science, University of Maragheh, P.O. Box 55136-83111, Maragheh, Iran. E-mail: ghodratmahmoudi@gmail.com
[b] Chemistry Department, Faculty of Engineering and Natural Sciences, Istinye University, Sarıyer, Istanbul 34396, Turkey
[c] Western Caspian University, Istiqlaliyyat Street 31, AZ 1001, Baku, Azerbaijan
[d] Departamento de Química Inorgánica, Facultad de Farmacia, Universidad de Santiago de Compostela, E-15782 Santiago de Compostela, Spain. E-mail: isabel.garcia@usc.es
[e] Department of Petroleum Engineering, Faculty of Engineering, University of Garmsar, Garmsar, Iran
[f] Departament de Quimica, Universitat de les Illes Balears, Crta de valldemossa km 7.5, 07122 Palma de Mallorca (Baleares), Spain
[g] University of Tyumen, Tyumen, 625003, Russian Federation. E-mail: damir.a.safin@gmail.com
[h] Scientific and Educational and Innovation Center for Chemical and Pharmaceutical Technologies, Ural Federal University named after the First President of Russia B.N. Yeltsin, Ekaterinburg, 620002, Russian Federation
† CCDC 2348187. For crystallographic data in CIF see DOI: 10.1039/x0xx00000x

Modern chemistry considers and utilizes a variety of noncovalent interactions as an efficient tool kit to design and dictate crystal structures. No doubt that among a rich pallet of noncovalent interactions, hydrogen bonding[10–12] and π-stacking interactions[13–15] are the most recognized and actively utilized ones. Suffice to mention, that both types of interactions play a pivotal role in the formation of DNA and RNA that are essential for all known forms of life. About a couple of decades ago a new concept of noncovalent interactions, viz. σ-hole, was introduced in chemistry.[16] Eventually, this concept was also spread to π-hole interactions and both have gained much attention as universal and effective structure-dictating tools. Within this concept, "holes" are regions on the atom with an electrons deficiency, which can potentially interact with an electron-rich atom. As such, a Lewis acid-base pair is formed.

A decade ago, a new type of σ-hole interactions, which is now known as tetrel bonding, was recognized.[17] This interaction involves elements of group 14 as an electron acceptor,[17,18] of which the Pb^{2+} cation, exhibiting a large radius and a rich variety of coordination numbers from 2 to 10, is of particular interest. Notably, the Pb^{2+} cation also exhibits a $6s^2$ lone-pair, which can influence to the formation of either holo- or hemidirectional coordination sphere.[19–22] The latter sphere can generate tetrel bonding. It should be noted, that lead has also been in the limelight of many studies on metal-based electrochemical reduction of CO_2.[23]

With all this in mind and in continuation of our comprehensive studies in the coordination chemistry of the hemidirected Pb^{2+} architectures as well in shedding light on the role of noncovalent interactions in the formation of extended structures,[24–41] we have concentrated on the *N'*-isonicotinoylpyrazine-2-carbohydrazonamide (**HL**),[42] which was intentionally designed to serve as a potentially bridging ligand, in the reaction with lead as a complexing agent. To shed light into the nature of the Pb···O tetrel bonds, the DFT calculations have been used along with MEP surface and QTAIM analyses.

2. Results and discussion

Oxidation of the lead anode under electrochemical conditions in the ambient atmosphere in a CH_3CN/MeOH solution of **HL** yielded a binuclear heteroleptic complex $[Pb_2L_2(CO_3)]\cdot 2CH_3CN\cdot 2MeOH$ (**1**·2CH_3CN·2MeOH) (Scheme 1), which orange plate-like crystals, suitable for X-ray studies, were formed by slow evaporation of the resulting solution.

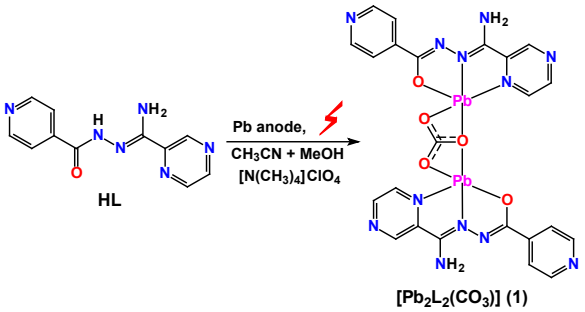

Scheme 1 Synthesis of **1**·2CH_3CN·2MeOH.

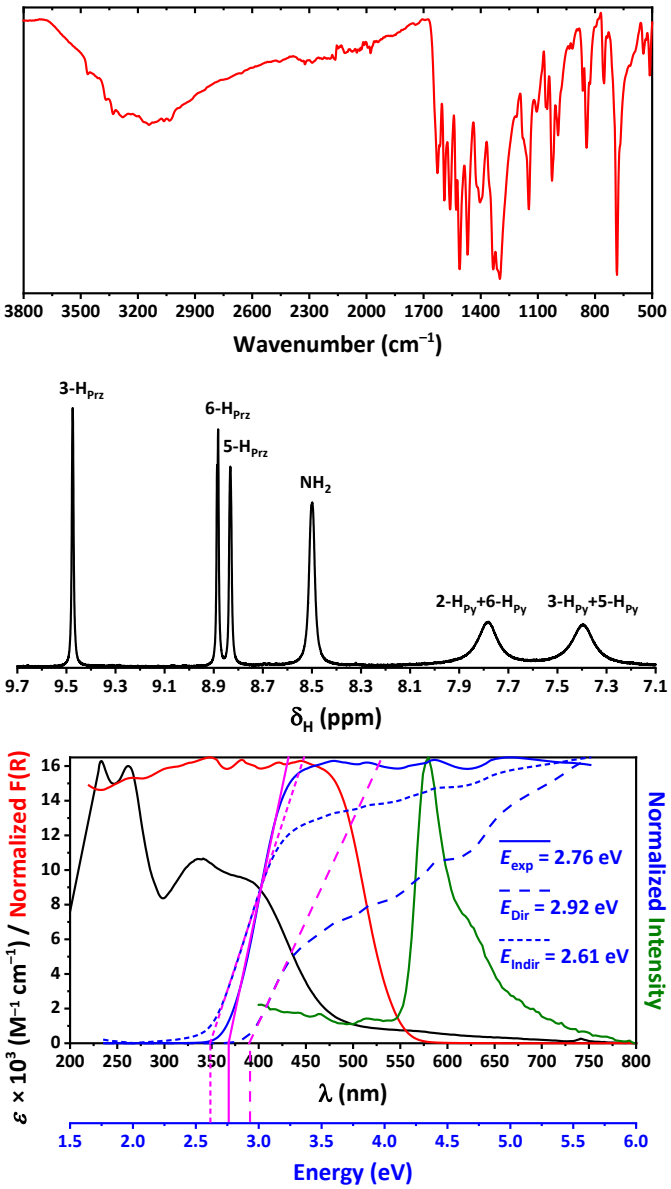

Fig. 1 (top) The IR, (middle) ^{1}H NMR, and (bottom) UV-vis (black), Kubelka-Munk (red and solid blue), $(\alpha h\nu)^2$ (dashed blue), $(\alpha h\nu)^{1/2}$ (short dashed blue) and luminescence (green) spectra of **1**·2CH_3CN·2MeOH.

The composition of the isolated compound was fully supported by the means of the elemental analysis data. The FTIR spectrum of complex revealed an intense band at about 1310 cm^{-1} corresponding to the CO_3^{2-} anion (Fig.1). The ^{1}H NMR spectrum of complex recorded in DMSO-d_6 supports the deprotonated form of the parent organic ligand in its structure due to the absence of the peak for the amide hydrogen atom (Fig. 1). In particular, the spectrum exhibits two broad singlets at 7.40 and 7.78 ppm corresponding to the pyridyl 3- and 5-, and 2- and 6-hydrogen atoms, respectively. The NH_2 protons were shown in the spectrum as a broad singlet at 8.50 ppm. Finally, the pyrazine hydrogen atoms were observed in the spectrum as three signals at 8.83, 8.88 and 9.48 ppm. The absorption spectrum of complex in MeOH contains bands up to about 720 nm with two intense maxima at 233 and 262 nm, and two

moderate maxima at 340 and 385 nm, of which the latter one is accompanied with a low intense shoulder spanning from about 500 nm to 720 nm (Fig.1). The diffuse reflectance spectrum of the title complex contains bands up to about 570 nm (Fig.1). The corresponding experimental, direct and indirect band gap values were calculated as 2.76, 2.92 and 2.61 eV, respectively.

Interestingly, the discussed complex was found to be emissive in a solution of MeOH upon excitation at 340 nm with a broad band from about 500 nm to 780 nm with a maximum at ~580 nm, accompanied with a shoulder at ~620 nm (Fig. 1). The CIE-1931 chromaticity coordinates of (0.28, 0.36) fall within the white gamut of the chromaticity diagram. Thus, complex **1** is a single-component white light-emitting phosphor. Comparison of the luminescence and absorption spectra of complex, as well as with the literature data allowed to assign the origin of the observed emission to a ligand-to-metal charge transfer (LMCT) excited state together with metal-centered (MC) transitions involving the s and p orbitals of Pb^{2+}.[25]

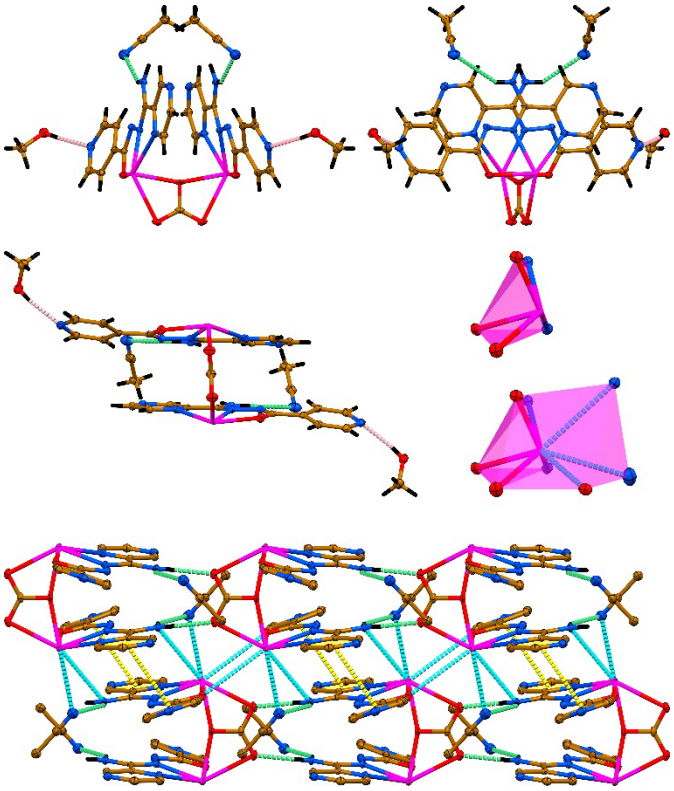

Fig. 2 (top and middle-left) Different views on the crystal structure of **1**·2CH_3CN·2MeOH. (middle right) Coordination polyhedra constructed from covalent (top), and covalent and tetrel bonds. (bottom) A supramolecular framework in the crystal structure of **1**·2CH_3CN·2MeOH, constructed through Pb···N and Pb···O tetrel bonds, N–H···N and N–H···O hydrogen bonds, and $\pi_{Pyrazine}\cdots\pi_{Pyridine}$ interactions (hydrogen atoms, except NH_2 groups, are omitted for clarity). Displacement ellipsoids are drawn with the 50% probability. Color code: H = black, C = gold, N = blue, O = red, Pb = magenta; Pb···N and Pb···O tetrel bonds = cyan dashed line, N–H···N and N–H···O hydrogen bonds = green dashed line, O–H···N hydrogen bond = pink dashed line, $\pi_{Pyrazine}\cdots\pi_{Pyridine}$ interaction = yellow dashed line.

Complex **1**·2CH_3CN·2MeOH crystallized in monoclinic space group *C*2/*c* with a half of the complex molecule [$Pb_2L_2(CO_3)$] (**1**) and one molecule of acetonitrile and one molecule of methanol in the asymmetric unit cell. Each metal cation in **1** is chelated by the tridentate ligand **L** through the 2-pyrazine and imine nitrogen atoms, and carbonyl oxygen atom, yielding a mononuclear cation $[PbL]^+$ (Fig. 2). Two mononuclear cations $[PbL]^+$ are linked into a molecular species through a carbonate anion, which, in turn, acts as both the bridging ligand and a counterion (Fig. 2). The carbonate anion is symmetrically linked to two Pb^{2+} cations through all the oxygen atoms, of which two are monodentate and the third one exhibits a bridging bidentate coordination mode (Fig. 2). The metal cations in the structure of **1** are in a five-membered N_2O_3 coordination environment, formed by the covalent bonds (Fig. 2).

Table 1 Selected bond lengths (Å) and angles (°) in the molecular structure of **1**.

Bond length			
Pb1–O11$_{carbonate}$	2.3768(5)	Pb1···Pb1^{iii}	4.6785(5)
Pb1–O12$_{carbonate}$	2.6285(14)	C17–O17 (carbonyl)	1.297(2)
Pb1–O17$_{carbonyl}$	2.3242(15)	C16–N12 (imine)	1.316(2)
Pb1–N11$_{Prz}$	2.6882(16)	C17–N13 (amide)	1.315(2)
Pb1–N12$_{imine}$	2.3709(16)	C16–N16 (amine)	1.343(2)
Pb1···O17$_{carbonyl}^{i}$	3.5997(13)	N12–N13	1.389(2)
Pb1···N16b$_{amine}^{ii}$	3.5308(15)	C10–O11 (carbonate)	1.332(3)
Pb1···N1$_{acetonitrile}^{ii}$	3.316(2)	C10–O12 (carbonate)	1.269(2)
Bond angle			
O11–Pb1–O12	52.38(5)	O12–Pb1–N11	121.74(5)
O11–Pb1–O17	86.47(4)	O12–Pb1–N12	132.16(5)
O11–Pb1–N11	82.75(5)	O17–Pb1–N11	130.37(5)
O11–Pb1–N12	85.17(5)	O17–Pb1–N12	67.67(5)
O12–Pb1–O17	86.59(5)	N11–Pb1–N12	63.24(5)
Dihedral angle			
Pyrazine···Pyridine	14.92(9)		

Symmetry code: i) –*x*, 2 – *y*, 1 – *z*; ii) –*x*, 1 – *y*, 1 – *z*; iii) –*x*, *y*, 1/2 – *z*.

The Pb–O bond length with the carbonyl oxygen atom of **L** is 2.3242(15) Å, while the same bond lengths with the monodentate and bridging carbonate atoms are 2.6285(14) and 2.3768(5) Å, respectively (Table 1). The Pb–N bond formed with the 2-pyrazine nitrogen atom is 2.6882(16) Å, while the same bond with the imine nitrogen atom is about 0.32 Å shorter (Table 1). The C–O bond **L** is 1.297(2) Å, while the same bonds in the carbonate anion are 1.332(3) and 1.269(2) Å for the bridging and monodentate oxygen atoms, respectively. The imine, amide and amine C–N bonds in **L** are very similar and vary from 1.315(2) Å to 1.343(2) Å, while the N-N distance is slightly longer and of 1.389(2) Å. Finally, the Pb···Pb separation in **1** is about 4.68 Å. The bond angles around the metal cation in the five-membered chelate rings of the $[PbL]^+$ cation are similar and of 63.24(5)° and 67.67(5)°, while the same bond angle formed by the pyrazine nitrogen and carbonyl oxygen atoms is almost a sum of the mentioned angles and of 130.37(5)° (Table 1). The

bond angle around the metal cation in the four-membered ring formed by the carbonate anion is the smallest one and of 52.38(5)°. Interestingly, the bond angles around the Pb^{2+} cation formed by the bridging carbonate oxygen atom and donor atoms of the organic ligand **L** are similar and vary from 82.75(5)° to 86.47(4)°. The same angle formed by the monodentate carbonate and the carbonyl oxygen atoms is very similar and of 86.59(5)°, while the bond angles formed by the monodentate carbonate and the pyrazine and imine nitrogen atoms are 121.74(5)° and 132.16(5)°, respectively. The pyrazine and pyridine rings are only slightly rotated relative to each other as evidenced from the corresponding dihedral angle between their mean planes of 14.92(9)°.

The most intriguing finding is that the crystal structure of **1**·2CH_3CN·2MeOH is stabilized by Pb···O tetrel bonds of 3.5997(13) Å formed with the carbonyl oxygen atom of an adjacent complex molecule, by Pb···N tetrel bonds formed with the NH_2 nitrogen atom of the other complex molecule, and by the Pb···N tetrel bonds formed with the acetonitrile nitrogen atom (Fig. 2, Table 1). As a result, a 2D supramolecular sheet is formed, which is further stabilized by the N–H···N hydrogen bonds, formed between one of the NH_2 hydrogen atoms and the acetonitrile nitrogen atom, and by the N–H···O hydrogen bonds, formed between the second NH_2 hydrogen atom and the monodentate carbonate oxygen atom, and by the $\pi_{Pyrazine}\cdots\pi_{Pyridine}$ interactions (Fig. 2, Table 2). Notably, the second donor nitrogen site of the pyrazine ring does not participate in the coordination of the metal center but is involved in the formation of O–H···N hydrogen bonding with the trapped methanol molecules (Fig. 2, Table 2).

Table 2 Hydrogen bond and $\pi\cdots\pi$ interaction lengths (Å) and angles (°) in the crystal structure of **1**·2CH_3CN·2MeOH.

D–X···A	*d*(D–X)	*d*(X···A)	*d*(D···A)	∠(DXA)
O2–H2···N14^{i}	0.81	1.98	2.783(2)	171
N16–H16A···N1^{ii}	0.87	2.57	3.341(3)	148
N16–H16B···O12^{i}	0.91	1.88	2.770(2)	165
Cg1···Cg2	*d*(Cg1···Cg2)	α	β	γ
Pyrazine···Pyridine^{iv}	3.7253(11)	14.92(9)	34.6	19.7
Pyridine···Pyrazine^{iv}	3.7253(11)	14.92(9)	19.7	34.6

Symmetry code: i) *x*, 1 – *y*, –1/2 + *z*; ii) *x*, *y*, *z*; iii) *x*, –1 + *y*, *z*; iv) –*x*, 1 – *y*, 1 – *z*.

We have also shed some light, using theoretical studies, on the Pb···O tetrel bonds observed in the solid state of **1**, which drive the formation of self-assembled dimers. Initially, we computed the molecular electrostatic potential (MEP) surface to identify nucleophilic and electrophilic regions of the complex. The MEP surface shows a minimum at the carbonate oxygen atoms (–65.3 kcal/mol) and a maximum at the NH_2 groups (+73.4 kcal/mol) (Fig. 3). This distribution explains the formation of the N–H···O bonds (indicated by green dotted lines in Fig. 2), which facilitate the propagation of the molecule into 1D polymers. Additionally, the MEP surface is notably negative at the aromatic nitrogen atoms of the pyridine, which engage in interactions with two co-crystallized methanol solvent molecules. Furthermore, the MEP over the pyridine ring is negative (–6.3 kcal/mol), while it is positive over the pyrazine ring (+24.5 kcal/mol), elucidating the formation of $\pi_{Pyrazine}\cdots\pi_{Pyridine}$ interactions (indicated by yellow dotted lines in Fig. 2). The MEP at the Pb atom exhibits a positive value with anisotropy that becomes evident when a reduced scale is applied (top-right of Fig 3). This anisotropy highlights an intense σ-hole opposite the Pb1–$O12_{carbonate}$ bond (+25.7 kcal/mol). Remarkably, directly opposite to this bond, a Pb···N tetrel bond forms, which also contributes to the $\pi_{Pyrazine}\cdots\pi_{Pyridine}$ interaction (Fig. 2). This detailed MEP surface analysis provides insights into the electronic factors underpinning the structural organization of the described complex.

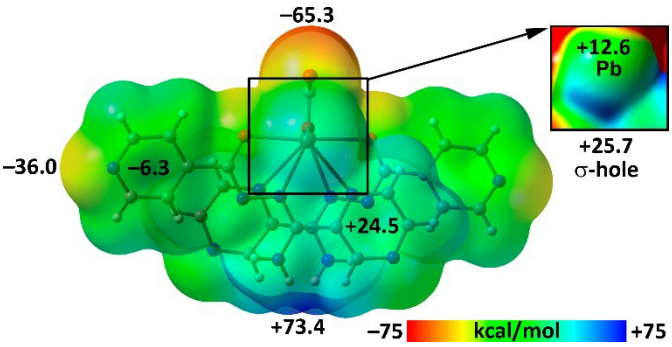

Fig. 3 The MEP surface of **1** at the PBE0-D4/def2-TZVP level of theory.

Using Quantum Theory of Atoms in Molecules (QTAIM) analysis, we have examined a centrosymmetric dimer stabilized by the Pb···O tetrel bonds (Fig. 4). The analysis shows that the monomers are interconnected by four bond critical points and bond paths, which link each Pb atom to two O atoms from the adjacent monomer. Consequently, the QTAIM analysis identifies the formation of two bifurcated tetrel bonds. This arrangement results in a dimerization energy of –13.5 kcal/mol, highlighting the significant role of tetrel bonds in the solid-state structure of **1**.

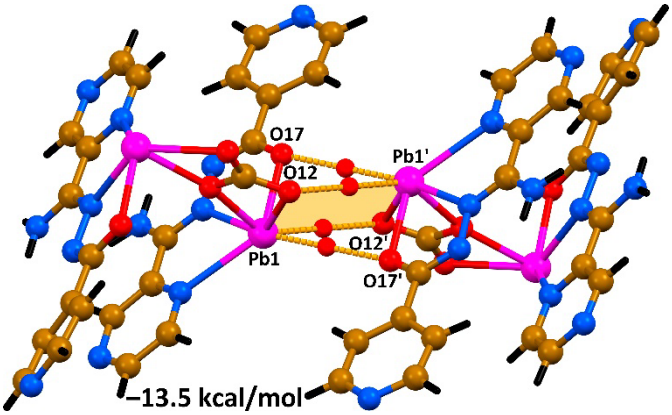

Fig. 4 QTAIM analysis of the dimer of **1** with the dimerization energy. Bond critical points are shown as small red spheres, while bifurcated Pb···O teterel bonds are shown as orange dashed lines. Only intermolecular interactions are shown (symmetry code: –*x*, *y*, 1/2 – *z*).

Further investigations were conducted to elucidate the attractive and noncovalent nature of the Pb···O contacts in the self-assembled dimer of **1** using a combined 2D plot of the Laplacian of electron density ($\nabla^2\rho$) overlaid with 2D reduced density gradient (RDG) maps (Fig. 5). The $\nabla^2\rho$ 2D plot offers insights into the covalency of the interaction, while the RDG maps effectively identify regions of noncovalent interactions, making these combined maps very convenient for a comprehensive understanding of the bonding characteristics. Additionally, the sign of the second eigenvalue of the Hessian matrix of $\nabla^2\rho$ (λ_2), within these low RDG regions, indicates the presence of attractive forces, further confirming the nature of the bond.

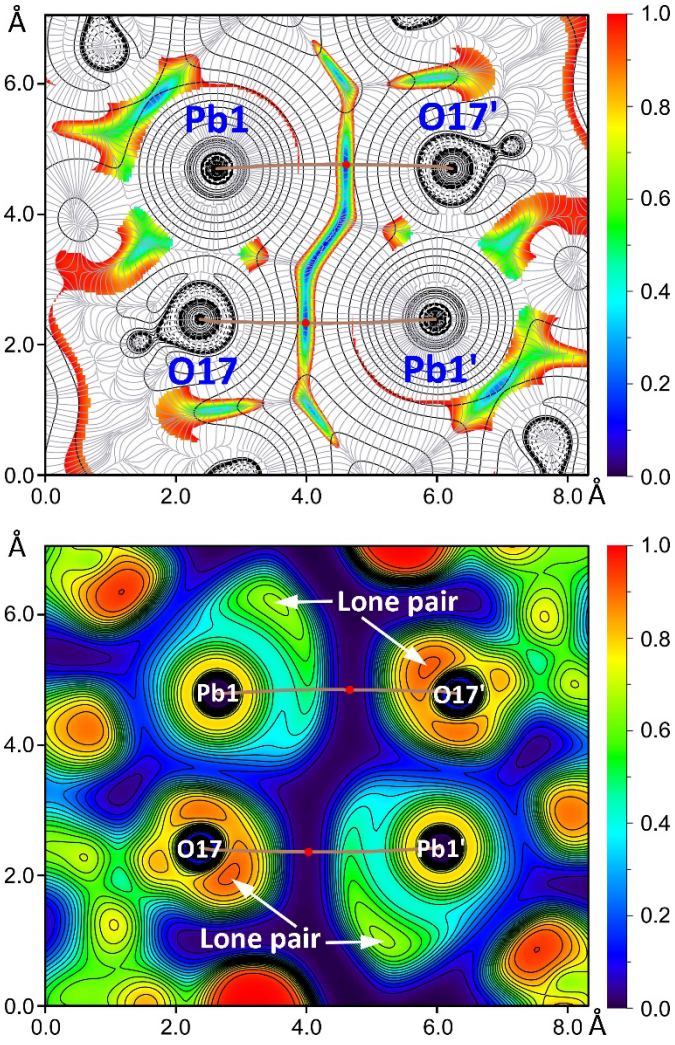

Fig. 5 (top) A 2D plot of the Laplacian (dashed and solid lines are for negative and positive values, respectively), including the gradient lines (in grey) overlapped with the 2D RDG map, and (bottom) a 2D ELF map for **1**. The 2D maps are represented in the plane defined by Pb1 and O17 atoms (symmetry code: –*x*, *y*, 1/2 – *z*). The bond paths are represented as brown lines and BCPs as red dots. The RDG density cut-off is 0.05 a.u.

The electron localization function (ELF) 2D map was also employed in this study to delineate the nucleophilic and electrophilic regions within the tetrel-bonded dimer (Fig. 5). This analysis is supplemented by the bond critical point (BCP) parameters (Table 3). Together, these analyses provide insight into the electronic interactions and stability characteristics of the Pb···O tetrel bonds in the dimer of **1**.

The 2D $\nabla^2\rho$ analysis displays positive values (represented by solid line isocontours) between the Pb and O atoms, illustrating both coordination bonds (Pb1–O17 and Pb1'–O17') and tetrel bonds (Pb1···O17' and Pb1'···O17). This distinction is further clarified by the 2D RDG map, which shows blue isocontours specifically in areas corresponding to the elongated Pb···O distances (tetrel bonds), effectively differentiating coordination bonds from tetrel bonds. The BCPs and bond paths that denote tetrel bonds are marked on the 2D maps, where the RDG values are near zero (Fig. 5). The ELF 2D map adds another level of detail, revealing the contrasting characteristics of Pb–O coordination and Pb···O tetrel bonds. It shows a peak in ELF at the lone pairs at the O atoms and underscores the electrophilic nature of the Pb atoms. The stereoactive lone pairs on the Pb atoms are also revealed by the ELF analysis, showing significantly lower ELF values (≈0.7) compared to those of the O atoms. This difference is attributed to the well-known inner lone pair effect. Moreover, the map indicates that areas between the Pb and O atoms connected by coordination bonds are colored blue (ELF ≈ 0.3), suggesting some degree of electron localization indicative of electron sharing. Conversely, regions associated with tetrel bonds, marked by BCPs in areas of minimal electron density (depicted in black), underscore the typical features of noncovalent interactions. This visualization confirms the weak noncovalent nature of the tetrel bonds.

Table 3 QTAIM and ELF values (a.u.) for the BCPs, characterizing the bifurcated tetrel bonds in **1**.

BCP	ρ(r)	G(r)	V(r)	∇2ρ(r)	ELF	λ_2
Pb1···O12	0.0033	0.0020	–0.0013	0.0107	0.0106	–0.0013
Pb1···O17	0.0047	0.0030	–0.0021	0.0160	0.0155	–0.0027

The QTAIM and ELF parameters at the Pb···O BCPs characterize the bifurcated tetrel bonds as weak (Table 3). This classification is supported by electron density (ρ) values below 0.005 a.u., positive and small values of the Laplacian of electron density ($\nabla^2\rho$), and the smaller absolute values of the potential energy density (|V|) compared to the kinetic energy density (G) at these BCPs. Furthermore, negative values of the second eigenvalue of the Hessian matrix (λ_2) in both cases indicate the presence of attractive forces. Comparative data highlight subtle differences between the tetrel bonds (Table 3); specifically, the ρ, ELF and λ_2 values are slightly higher for Pb1···O17. This is consistent with the shorter Pb1···O17' distance (3.600(1) Å) compared to Pb1···O12' (3.790(1) Å).

Conclusions

In the present contribution, we report synthesis and detailed analysis of the novel binuclear lead(II) complex $[Pb_2L_2(CO_3)]\cdot 2CH_3CN\cdot 2MeOH$ (**1**·$2CH_3CN$·2MeOH), which was readily obtained from *N'*-isonicotinoylpyrazine-2-

carbohydrazonamide (**HL**) by electrochemical oxidation of a lead anode in a CH_3CN:MeOH solution. The carbonate anion was formed from conversion of the aerial carbon dioxide by the lead(II)–**L** complex system under electrochemical conditions, followed by its trapping in the structure of **1**. In **1**, the ligands **L** exhibits a tridentate coordination mode through the pyrazine and imine nitrogen atoms, and the carbonyl oxygen atom, while the carbonate anion exhibits a tetradentate bridging coordination mode, linking two complex cations $[PbL]^+$. In the carbonate anion two oxygen atoms are linked to two neighbouring metal cations, while the third oxygen atom links the same metal two cations in a bridging bidentate coordination mode. The molecular structure of **1** is stabilized by the Pb···N and Pb···O tetrel bonds, yielding a 2D supramolecular sheet. The resulting sheet is further stabilized by N–H···N and N–H···O hydrogen bonds, and $\pi_{Pyrazine}\cdots\pi_{Pyridine}$ interactions. The DFT study has demonstrated that the Pb···O tetrel bonds play a crucial role in stabilizing and defining the electronic architecture of the studied dimers, with their noncovalent nature and interaction strength comparable to that of strong hydrogen bonds. A solution of the obtained complex in MeOH absorbs up to about 500 nm with intense and moderate maxima, accompanied with a "tail" up to about 720 nm. The solid material of the obtained complex exhibits bands up to about 570 nm in the corresponding diffuse reflectance spectrum with the experimental, direct and indirect band gap values of 2.76, 2.92 and 2.61 eV, respectively. Finally, the same solution of the discussed complex in MeOH was found to be emissive with a broad band from about 500 nm to 780 nm and with a maximum at ~580 nm, accompanied with a shoulder at ~620 nm. The CIE-1931 chromaticity coordinates of (0.28, 0.36) were found to be within the white gamut of the chromaticity diagram, indicating that complex **1** is a single-component white light-emitting phosphor.

Experimental

Materials and physical measurements

All reagents and solvents were commercially available and used as without further purification. **HL** was synthesized according to the recently described procedure using isonicotinohydrazide and 2-cyanopyrazine.[42] The FTIR spectra were recorded on a FT Varian FT-IR 670 spectrometer, equipped with an attenuated total reflectance (ATR) accessory, in the 500–4000 cm^{-1} range. The ^1H NMR spectrum in DMSO-d_6 was recorded with a Bruker DPX FT/NMR-400 spectrometer. The absorption and fluorescence spectra were recorded from a freshly prepared solution of complex in a freshly distilled MeOH using a Jasco V-770 spectrophotometer and Edinburgh Instruments FS5 spectrofluorometer, respectively. Elemental analyses were performed on a Thermo Scientific FlashSmart analyzer.

Synthesis

The complex was obtained using an electrochemical procedure. The cell consisted of a tall-form beaker (100 mL) fitted with a rubber bung through which the electrodes entered. An acetonitrile solution of **HL**, containing a few mg of $[N(CH_3)_4]ClO_4$ as a current carrier, was electrolyzed using a platinum wire as the cathode and a metal plate as the sacrificial anode (**Caution!** *Although problems were not encountered in this work, all perchlorate compounds are potentially explosive, and should be handled in small quantities and with great care!*). The applied voltage allowed a sufficient current flow for smooth dissolution of the metal. The current was maintained at 5 mA for 0.5 h. During the electrolysis hydrogen was evolved at the cathode. Under these conditions the cell can be summarized as $Pb_{(+)}$/**HL** + $CH_3CN/Pt_{(-)}$.

1·2CH₃CN·2MeOH. Electrochemical oxidation of a lead anode under the ambient atmosphere in a solution of **HL** (0.051 g, 0.21 mmol) in CH_3CN:MeOH (1:1, 80 mL) at 7 V and 5 mA for 0.5 h caused 9.5 mg of lead to be dissolved, E_f = 0.50 mol/F. Orange plate-like crystals, suitable for X-ray studies, were obtained by slow evaporation of the resulting solution. Yield: 24.4 mg (96.3%). Anal. calc. for $C_{29}H_{32}N_{14}O_7Pb_2$ (1103.06): C 31.58, H 2.92 and N 17.78%; found: C 31.47, H 2.84 and N 17.86%.

X-ray diffraction analysis

The X-ray diffraction data were collected at 100(2) K on a Bruker D8 VENTURE PHOTON III-14 diffractometer (Mo-Kα, λ = 0.71073 Å, graphite monochromator). The data were processed with APEX4[43] and corrected for absorption using SADABS.[44] The structure was solved by direct methods using the program SHELXS-2013[45] and refined by the full-matrix least-squares technique using SHELXL-2013.[45] All hydrogen atom positions located on a difference map and included as fixed contributions riding on attached atoms with isotropic thermal parameters 1.2 times those of their carrier atoms.

Crystal data for 1·2CH₃CN·2MeOH: $C_{23}H_{18}N_{12}O_5Pb_2$, $2(C_2H_3N)$, $2(CH_4O)$; M_r = 1103.06 g mol^{-1}, monoclinic, space group $C2/c$, a = 26.8255(16), b = 9.3424(6), c = 13.8939(8) Å, β = 93.608(2)°, V = 3475.1(4) $Å^3$, Z = 4, ρ = 2.108 g cm^{-3}, μ(Mo-Kα) = 9.744 mm^{-1}, reflections: 101368 collected, 5310 unique, R_{int} = 0.047, R_1(all) = 0.0164, wR_2(all) = 0.0353, S = 1.062.

Theoretical calculations

The geometry of complex was computed at the PBE0-D4/def2-TZVP level of theory,[46–48] using the crystallographic coordinates within the Turbomole 7.7 program.[49] The "atoms-in-molecules" (AIM)[50] analysis of the electron density has been performed at the same level of theory using the Multiwfn program.[51] The reduced density gradient (RDG)[52] and electron localization function (ELF)[53] 2D plots were computed using the Multiwfn program.[51] The QTAIM analysis was represented using the VMD software.[54] The Laplacian of electron density can be decomposed into the sum of contributions along the three principal axes of maximal variation, giving the three eigenvalues of the Hessian matrix (λ_1, λ_2 and λ_3). The sign of λ_2 can be utilized to distinguish bonding (attractive, $\lambda_2 < 0$) weak interactions from non-bonding ones (repulsive, $\lambda_2 > 0$).[52]

Conflicts of interest

There are no conflicts to declare.

Funding

This work was funded by the grant from the Russian Science Foundation (No. 24-23-00118).

Notes and references

1 P. Falkowski, R. J. Scholes, E. Boyle, J. Canadell, D. Canfield, J. Elser, N. Gruber, K. Hibbard, P. Högberg, S. Linder, F. T. Mackenzie, B. Moore III, T. Pedersen, Y. Rosenthal, S. Seitzinger, V. Smetacek and W. Steffen, The Global Carbon Cycle: A Test of Our Knowledge of Earth as a System, *Science*, 2000, **290**, 291.

2 D. W. Keith, Why Capture CO_2 from the Atmosphere? *Science*, 2009, **325**, 1654.

3 F. Parrenin, V. Masson-Delmotte, Köhler, D. Raynaud, D. Paillard, J. Schwander, C. Barbante, A. Landais, A. Wegner and J. Jouzel, Synchronous Change of Atmospheric CO_2 and Antarctic Temperature During the Last Deglacial Warming, *Science*, 2013, **339**, 1060.

4 T. Sakakura, J.-C. Choi and H. Yasuda, Transformation of Carbon Dioxide, *Chem. Rev.*, 2007, **107**, 2365.

5 J.-M. Savéant, Molecular Catalysis of Electrochemical Reactions. Mechanistic Aspects, *Chem. Rev.*, 2008, **108**, 2348.

6 C. Liu, T. R. Cundari and A. K. Wilson, Periodic Trends in 3d Metal Mediated CO_2 Activation, in A*pplications of Molecular Modeling to Challenges in Clean Energy*, ed. G. Fitzgerald and N. Govind, 2013, ACS Symposium Series; American Chemical Society: Washington, DC, USA, p. 67.

7 E. Lamy, L. Nadjo, J. M. Savéant, Standard potential and kinetic parameters of the electrochemical reduction of carbon dioxide in dimethylformamide, *J. Electroanal. Chem.*, 1977, **78**, 403.

8 C. Amatore and J.-M. Saveant, Mechanism and kinetic characteristics of the electrochemical reduction of carbon dioxide in media of low proton availability, *J. Am. Chem. Soc.*, 1981, **103**, 5021.

9 H. A. Schwarz and R. W. Dodson, Reduction potentials of CO_2 and the alcohol radicals, *J. Phys. Chem.*, 1989, **93**, 409.

10 J. O. T. W, Hydrogen bonding : S.N. Vinogradov and R.H. Linnell, Van Nostrand Reinhold Company, London, 1971, pp. 319, price £4.75, *J. Mol. Struct.*, 1972, **14**, 470.

11 G. R. Desiraju, Reflections on the Hydrogen Bond in Crystal Engineering, *Cryst. Growth Des.*, 2011, **11**, 896.

12 S. J. Grabowski, Analysis of Hydrogen Bonds in Crystals, *Crystals*, 2016, **6**, 59.

13 C. A. Hunter and J. K. M. Sanders, The nature of π–π interactions, *J. Am. Chem. Soc.*, 1990, **112**, 5525.

14 K. Müller-Dethlefs and P. Hobza, Noncovalent Interactions: A Challenge for Experiment and Theory, *Chem. Rev.*, 2000, **100**, 143.

15 C. Janiak, A critical account on π–π stacking in metal complexes with aromatic nitrogen-containing ligands, *J. Chem. Soc. Dalton Trans.*, 2000, 3885.

16 T. Clark, M. Hennemann, J. S. Murray and P. Politzer, Halogen bonding: the σ-hole, *J. Mol. Model.*, 2007, **13**, 291.

17 Special Issue "Tetrel Bonds", https://www.mdpi.com/journal/molecules/special_issues/Tetrel_Bonds

18 L. Shimoni-Livny, J. P. Glusker and C. W. Bock, Lone Pair Functionality in Divalent Lead Compounds, *Inorg. Chem.*, 1998, **37**, 1853.

19 A. Bauzá, T. J. Mooibroek and A. Frontera, Tetrel Bonding Interactions, *Chem. Rec.*, 2016, **16**, 473.

20 A. Bauzá, S. K. Seth and A. Frontera, Tetrel bonding interactions at work: Impact on tin and lead coordination compounds, *Coord. Chem. Rev.*, 2019, **384**, 107.

21 I. Alkorta, J. Elguero and A. Frontera, Not Only Hydrogen Bonds: Other Noncovalent Interactions, *Crystals*, 2020, **10**, 180.

22 Z. Yang, F. E. Oropeza and K. H. L. Zhang, P-block metal-based (Sn, In, Bi, Pb) electrocatalysts for selective reduction of CO_2 to formate, *APL Mater.*, 2020, **8**, 060901.

23 G. Mahmoudi, A. Bauzá, M. Amini, E. Molins, J. T. Mague and A. Frontera, On the importance of tetrel bonding interactions in lead(ii) complexes with (iso)nicotinohydrazide based ligands and several anions, *Dalton Trans.*, 2016, 45, 10708.

24 G. Mahmoudi, A. V. Gurbanov, S. R. Hemida, R. Corballo, M. Amini, A. Bacchi, M. P. Mitoraj, F. Sagan, M. Kukulka and D. A. Safin, Ligand-Driven Coordination Sphere-Induced Engineering of Hybride Materials Constructed from PbCl2 and Bis-Pyridyl Organic Linkers for Single-Component Light-Emitting Phosphors, *Inorg. Chem.*, 2017, **56**, 9698.

25 G. Mahmoudi, A. A. Khandar, J. White, M. P. Mitoraj, H. S. Jena, P. Van Der Voort, N. Qureshi, A. M. Kirillov, K. Robeyns and D. A. Safin, Polar protic solvent-trapping polymorphism of the Hg^{II}-hydrazone coordination polymer: experimental and theoretical findings, *CrystEngComm*, 2017, **19**, 3017.

26 G. Mahmoudi, D. A. Safin, M. P. Mitoraj, M. Amini, M. Kubicki, T. Doert, F. Locherere and M. Fleck, Anion-driven tetrel bond-induced engineering of lead(II) architectures with *N*′-(1-(2-pyridyl)ethylidene)nicotinohydrazide: experimental and theoretical findings, *Inorg. Chem. Front.*, 2017, **4**, 171.

27 G. Mahmoudi, E. Zangrando, M. P. Mitoraj, A. V. Gurbanov, F. I. Zubkov, M. Moosavifar, I. A. Konyaeva, A. M. Kirillov and D. A. Safin, Extended lead(II) architectures engineered *via* tetrel bonding interactions, *New J. Chem.*, 2018,**42**, 4959.

28 G. Mahmoudi, F. A. Afkhami, A. Kennedy, F. I. Zubkov, E. Zangrando, A. M. Kirillov, E. Molins, M. P. Mitoraj and D. A. Safin, Lead(II) coordination polymers driven by pyridine-hydrazine donors: from anion-guided self-assembly to structural features, *Dalton Trans.*, 2020, **49**, 11238.

29 F. A. Afkhami, G. Mahmoudi, F. Qu, A. Gupta, M. Köse, E. Zangrando, F. I. Zubkov, I. Alkorta and D. A. Safin, Supramolecular lead(II) architectures engineered by tetrel bonds, *CrystEngComm*, 2020, **22**, 2389.

30 G. Mahmoudi, M. Abedi, S. E. Lawrence, E. Zangrando, M. G. Babashkina, A. Klein, A. Frontera and D. A. Safin, Tetrel Bonding and Other Non-Covalent Interactions Assisted Supramolecular Aggregation in a New Pb(II) Complex of an Isonicotinohydrazide, *Molecules*, 2020, **25**, 4056.

31 G. Mahmoudi, F. A. Afkhami, E. Zangrando, W. Kaminsky, A. Frontera and D. A. Safin, A supramolecular 3D structure constructed from a new metal chelate self-assembled from $Sn(NCS)_2$ and phenyl(pyridin-2-yl)methylenepicolinohydrazide, *J. Mol. Struct.*, 2020, **49**, 129188.

32 G. Mahmoudi, M. Kubicki, D. Choquesillo-Lazarte, B. Miroslaw, E. V. Alexandrov, P. N. Zolotarev, A. Frontera and D. A. Safin, Supramolecular architectures of $Mn(NCS)_2$ complexes with *N*′-(1-(pyridin-4-yl)ethylidene)picolinohydrazide and *N*′-(phenyl(pyridin-4-yl)methylene)isonicotinohydrazide, *Polyhedron*, 2020, **190**, 114776.

33 F. A. Afkhami, G. Mahmoudi, F. Qu, A. Gupta, E. Zangrando, A. Frontera and D. A. Safin, Supramolecular architecture constructed from the hemidirected lead(II) complex with *N*′-(4-hydroxybenzylidene)isonicotinohydrazide, *Inorg. Chim. Acta*, 2020, **502**, 119350.

34 J. D. Velásquez, G. Mahmoudi, E. Zangrando, B. Miroslaw, D. A. Safin and J. Echeverría, Non-covalent interactions induced supramolecular architecture of $Hg(NCS)_2$ with 3-pyridinecarbaldehyde nicotinoylhydrazone, *Inorg. Chim. Acta*, 2020, **509**, 119700.

35 G. Mahmoudi, A. Masoudiasl, F. A. Afkhami, J. M. White, E. Zangrando, A. V. Gurbanov, A. Frontera and D. A. Safin, A new coordination polymer constructed from $Pb(NO_3)_2$ and a benzylideneisonicotinohydrazide derivative: Coordination-induced generation of a π-hole towards a tetrel-bonding stabilized structure, *J. Mol. Struct.*, 2021, **1234**, 130139.

36 I. Garcia-Santos, A. Castiñeiras, G. Mahmoudi, M. G. Babashkina, E. Zangrando, R. M. Gomila, A. Frontera and D. A. Safin, Supramolecular aggregation of lead(II) perchlorate and a thiosemicarbazide derivative linked by a myriad of non-covalent interactions, *Inorg. Chim. Acta*, 2022, **538**, 120974.

37 G. Mahmoudi, I. Garcia-Santos, M. Pittelkow, F. S. Kamounah, E. Zangrando, M. G. Babashkina, A. Frontera and D. A. Safin, The tetrel bonding role in supramolecular aggregation of lead(II) acetate and a thiosemicarbazide derivative, *Acta Cryst.*, 2022, **B78**, 685.

38 I. Garcia-Santos, A. Castiñeiras, G. Mahmoudi, M. G. Babashkina, E. Zangrando, R. M. Gomila, A. Frontera and D. A. Safin, An extended supramolecular coordination compound produced from $PbCl_2$ and *N*′-isonicotinoylpicolinohydrazonamide, *CrystEngComm*, 2022, **24**, 368.

39 G. Mahmoudi, E. Zangrando, A. V. Gurbanov, B. Eftekhari-Sis, M. P. Mitoraj, F. Sagan and D. A. Safin, Tetrel bonding stabilization of a new coordination polymer constructed from lead(ii) azide and 1-(pyridin-2-yl)ethylidenepicolinohydrazide, *CrystEngComm*, 2023, **25**, 5100.

40 B. Eftekhari-Sis, I. Garcia-Santos, A. Castiñeiras, G. mahmoudi, E. Zangrando, A. Frontera and D. A. Safin, On the pivotal role of tetrel bonding in the supramolecular architectures of Pb^{II}–NCS complexes with chelating thiosemicarbazide derivatives, *CrystEngComm*, 2024, **26**, 1637.

41 I. Garcia-Santos, A. Castiñeiras, B. Eftekhari, Sis, G. Mahmoudi and D. A. Safin, *N*′-isonicotinoylpicolinohydrazonamide: Synthesis, crystal structure, DFT and ADMET studies, and in silico inhibition properties toward a series of COVID-19 proteins, *Polyhedron*, 2023, **235**, 116362.

42 APEX4 Software, Bruker AXS Inc. v2021.10-0, Madison, Wisconsin, USA, 2021.

43 G. M. Sheldrick, SADABS. Bruker AXS Inc., Madison, WI-53719, USA, 1997.

44 G. M. Sheldrick, A short history of *SHELX*, *Acta Cryst.*, 2008, **A64**, 112.

45 C. Adamo and V. Barone, Toward reliable density functional methods without adjustable parameters: The PBE0 model, *J. Chem. Phys*., 1999, **110**, 6158.

46 F. Weigend, Accurate Coulomb-fitting basis sets for H to Rn, *Phys. Chem. Chem. Phys.*, 2006, **8**, 1057.

47 E. Caldeweyher, C. Bannwarth and S. Grimme, Extension of the D3 dispersion coefficient model, *J. Chem. Phys*., 2017, **147**, 034112.

48 R. Ahlrichs, M. Bär, M. Häser, H. Horn and C. Kölmel, Electronic structure calculations on workstation computers: The program system turbomole, *Chem. Phys. Let*., 1989, **162**, 165.

49 R. F. W. Bader, A quantum theory of molecular structure and its applications, *Chem. Rev*., 1991, **91**, 893.

50 T. Lu and F. Chen, Multiwfn: A multifunctional wavefunction analyzer, *J. Comput Chem*., 2012, **33**, 580.

51 J. Contreras-Garcia, E. R. Johnson, S. Keinan, R. Chaudret, J.-P. Piquemal, D. N. Beratan and W. Yang, NCIPLOT: A Program for Plotting Noncovalent Interaction Regions, *J. Chem. Theory Comput*., 2011, **7**, 625.

52 A. D. Becke and K. E. Edgecombe, A simple measure of electron localization in atomic and molecular systems, *J. Chem. Phys*., 1990, **92**, 5397.

53 W. Humphrey, A. Dalke and K. Schulten, VMD: visual molecular dynamics, *J. Mol. Graph*., 1996, **14**, 33.

